









## Thermodynamic Structure of the Solar Corona: Tomographic Reconstructions and MHD Modeling

Diego G. Lloveras<sup>1</sup>  · Alberto  
M. Vásquez<sup>1,2</sup>  · Federico A. Nuevo<sup>1,3</sup>  ·  
Cecilia Mac Cormack<sup>1,2</sup>  ·  
Nishtha Sachdeva<sup>4</sup>  · Ward Manchester  
IV<sup>4</sup>  · Bartholomeus Van der Holst<sup>4</sup>  ·  
Richard A. Frazin<sup>4</sup> 

© Springer ....

**Abstract** Observational techniques play an essential role in advancing our understanding of the physics of the solar corona, providing in particular validation

- 
- ✉ D.G. Lloveras  
dlloveras@iafe.uba.ar
  - ✉ A.M. Vásquez  
albert@iafe.uba.ar
  - ✉ F.A. Nuevo  
federico@iafe.uba.ar
  - ✉ C. Mac Cormack  
cmaccormack@iafe.uba.ar
  - ✉ N. Sachdeva  
nishthas@umich.edu
  - ✉ W. Manchester IV  
chipm@umich.edu
  - ✉ B. Van der Holst  
bartvand@umich.edu
  - ✉ R.A. Frazin  
rfrazin@umich.edu

<sup>1</sup> Instituto de Astronomía y Física del Espacio (IAFE), CONICET-UBA, CC 67 - Suc 28, (C1428ZAA) Ciudad Autónoma de Buenos Aires, Argentina

<sup>2</sup> Universidad Nacional de Tres de Febrero (UNTREF). Departamento de Ciencia y Tecnología, Sáenz Peña, Argentina.

<sup>3</sup> Ciclo Básico Común (CBC), Universidad de Buenos Aires (UBA), Buenos Aires, Argentina

<sup>4</sup> Department of Climate and Space Sciences and Engineering (CLaSP), University of Michigan, 2455 Hayward Street, Ann Arbor, MI 48109-2143, USA

data for three-dimensional (3D) magnetohydrodynamic (MHD) models of the solar atmosphere. Solar rotational tomography is currently the sole observational technique that provides a 3D quantitative description of the solar corona at a global scale. Based on extreme ultraviolet data of space borne instruments, differential emission measure tomography (DEMT) allows constructing 3D maps of the coronal electron density and temperature at heliocentric heights below  $\approx 1.25 R_{\odot}$ . We carry out a study of the corona combining DEMT reconstructions with MHD simulations using the latest version of the Alfvén Wave Solar Model (AWSoM) of the Space Weather Modeling Framework. Target rotations were selected from the solar minimum between solar cycles (SC) 23 and 24 and the declining phase of SC 24. The 3D tomographic and MHD models are analysed and compared in distinct coronal magnetic structures. We report in quantitative detail on the 3D thermodynamic structure of the inner corona as revealed by the DEMT analysis. We show in particular the existence of diverse types of temperature structures in the low and mid latitudes of the streamer belt, and that the heating energy required to keep them stable may be accounted for by Alfvén waves. We show that the latest version of the AWSoM model results agree with DEMT reconstructions to within a  $\approx 20\%$  accuracy or better. We report on aspects of the AWSoM model that could be improved to better reproduce the DEMT results, in particular concerning the source region of the fast/slow solar winds.

**Keywords:** Solar Cycle, Observations; Corona,E; Corona, Structures

## 1. Introduction

Being the region where the solar atmosphere is heated, solar wind accelerated, and where impulsive events such as solar flares and coronal mass ejections are energized, observation and modeling of the solar corona are tasks of great relevance to improve our understanding of the Sun-Earth environment. To advance our knowledge of the physics of the solar corona, as well as to improve its three-dimensional (3D) models, information derived from observational data plays a key role. Solar rotational tomography (SRT) is currently the sole observational technique able to provide a quantitative empirical description of the 3D distribution of some fundamental plasma parameters of the solar corona at a global scale.

To study the global coronal 3D structure, SRT proved to be a powerful tool. Based on solar rotation, allow instruments to compile a time series of images that cover the entire corona collecting data from all lines of sight. In particular, differential emission measure tomography (DEMT), based on time-series of extreme ultraviolet (EUV) images, allows reconstruction of the 3D distribution of the differential emission measure (DEM) of the quiet-Sun low corona at a global scale. The technique was first developed by Frazin, Vásquez, and Kamalabadi (2009), and first applied to the observational study of coronal structures by Vásquez, Frazin, and Kamalabadi (2009). Using solar rotation time series of EUV images taken in channels sensitive to different temperatures, the technique allows

calculation of 3D maps of electron density and temperature in the heliocentric height range  $1.0 R_{\odot}$  to  $1.2 R_{\odot}$  as summarized in Section 2.1. The reader may refer to the recent review by Vázquez (2016) that summarizes the DENT technique.

A combination of the DENT and global magnetic models has provided useful insight into the 3D thermodynamical structure of the global quiet-Sun corona. In previous works, DENT has been combined with a potential field source surface (PFSS) model such as Huang *et al.* (2012), Nuevo *et al.* (2013) and Nuevo *et al.* (2015). Recently, Lloveras *et al.* (2017) combined DENT with PFSS to study the thermodynamic of the last two solar minima along magnetic field lines and selecting different magnetic structures and Mac Cormack *et al.* (2017) developed a new DENT product concerning the energetics of the inner solar corona through PFSS magnetic lines.

The Alfvén Wave Solar atmosphere Model (AWSoM) is a three-dimensional (3D) physics-based, data-driven model extending from the upper chromosphere, into the solar corona upto 1 AU (and beyond) (van der Holst *et al.*, 2010, 2014) and is constantly validated with observations as new improvements are implemented. DENT results were used by Jin *et al.* (2012) and Oran *et al.* (2015) to validate AWSoM results finding an agreement within 50% in density and electron temperature in the low corona. More recently, Sachdeva *et al.* (2019) compared the results of the latest version of AWSoM model with DENT products in a globally fashion, obtaining an agreement within 20%. We used AWSoM results with two purposes. On the one hand to provide thermodynamic results to be contrasted with DENT, and on the other hand to provide magnetohydrodynamic (MHD) coronal magnetic field model that is used to study thermodynamics along field lines.

We carry out a quantitatively detailed comparative DENT/AWSoM analysis of the Carrington Rotation (CR)-2082 during the Solar Cycle (SC) 23/24 minimum and CR-2208 during the declining fase of SC 24. To study CR-2082 data taken by the *Extreme UltraViolet Imager Behind* (EUVI-B (Wuelser *et al.*, 2004)) on board the *Solar TERrestrial RELations Observatory* (STEREO) was used for DENT, and Global Oscillation Network Group (GONG) magnetogram as the only input for AWSoM, while data taken by the *Atmospheric Imaging Assembly instrument* (AIA (Lemen *et al.*, 2012)), on board the *Solar Dynamics Observatory* (SDO) mission was used to study CR-2208 for DENT, and Air Force Data Assimilation Photospheric flux Transport (ADAPT)-GONG magnetograms for AWSoM.

Section 2.1 and 2.2 summarizes DENT technique, AWSoM model, instruments, and datasets we used. Section 2.3 explains the technique that is used to trace the thermodynamic results along the field lines. Section 2.4 details the energy model and the loop integrated quantities that are part of the comparative analysis. In Section 3.1 the quantitative comparative analysis of both rotations using DENT is described and in Section 3.2 AWSoM results are related to the one of DENT. Finally in Section 4 summarizes and discusses the main conclusions of this analysis, and anticipates further planned work.

## 2. Methodology

### 2.1. DENT Reconstructions

We carried out the 3D DENT reconstruction and MHD modeling of two target Carrington rotations (CR). We selected CR-2082 (2009, 05 April through 03 May), a deep minimum rotation between solar cycles (SC) 23 and 24, and CR-2208 (2018, 02 September through 29 September), a rotation during the early declining phase of SC 24. To study CR-2082 and CR-2208 data taken by the STEREO/EUVI-B and SDO/AIA instruments was used, respectively. The EUVI and AIA data were prepared using the latest processing tools and calibration corrections provided by their teams through the SolarSoft package. For this work, we introduced two improvements in the implementation of the DENT technique, as described next.

While in all previous DENT studies full-disk data was used to perform tomography, in this work we opted to only use off-limb data. In this way, the smallest scale and brighter coronal features seen on disk (most typically in the 171Å band) are not included. This has two implications. Firstly, the fast dynamics that typically characterizes those structures is absent from the data. Secondly, only half synodic rotation worth of data is needed to constrain the inversion problem for the whole coronal volume. As a result, coronal dynamics induced artifacts are reduced compared to previous DENT reconstructions.

The solution of the tomographic problem involves a very large sparse matrix. Such type of inversion problems are characterized by spurious high-frequency artifacts in the solution, which can be mitigated through *regularization* techniques (Frazin, 2000). In the case of DENT, all previous efforts used the 2D scheme implemented by Frazin, Vásquez, and Kamalabadi (2009), using a finite difference matrix operator to approximate angular derivatives in both latitude and longitude. Also new to the present work, is the implementation of an expanded 3D regularization scheme, which adds to the previous scheme a finite difference matrix operator to approximate radial derivatives. In this way, the tomographic inversion problem is performed penalizing nonphysical high-frequency artifacts in all three spatial directions. As a result, tomographic reconstructions behave more smoothly close to the radial boundaries of the computational grid when compared to previous reconstructions. The size of the tomographic grid cell (or voxel) is typically set to  $0.01 R_{\odot}$  in the radial direction (covering the height range  $1.0 - 1.25 R_{\odot}$ ) and  $2^{\circ}$  in both the latitudinal and longitudinal directions.

We summarize next the main aspects of DENT required for the analysis of this work. We refer the reader to Frazin, Vásquez, and Kamalabadi (2009) for a full description of the technique.

In a first step, the time series of EUV images is used to solve a solar rotational tomography (SRT) problem, for each EUV band independently. As a result, the 3D distribution of the so called *filter band emissivity* (FBE) is determined for each band separately. The FBE, an emissivity-type quantity, is defined as the wavelength integral of the coronal EUV spectral emissivity and the telescope's passband function of each EUV channel. Line-of-sight (LOS) integration of the FBE provides synthetic images that can be quantitatively compared to the real

data in the time series. To find the FBE, the tomographic problem is posed a global optimization problem in which the quadratic norm of the difference between all pairs of synthetic and real images is minimized.

In a second step, the FBE values obtained for all bands in each voxel of the tomographic grid are used to constrain the determination of the LDEM which, as described in Section 1, describes the temperature distribution of the plasma within the individual voxel. Specifically, at each tomographic voxel  $i$ , the FBE of the band  $k$  is related to the LDEM of the voxel according to

$$\text{FBE}_i^{(k)} = \int dT \text{LDEM}_i(T) \text{TRF}^{(k)}(T), \quad k = 1, \dots, K \quad (1)$$

where  $K$  is the number EUV bands, and  $\text{TRF}^{(k)}$  is the *temperature response function* of the  $j$ -th detector. The TRFs are here computed based on the (known) channel's passband times the coronal emissivity at that temperature (normalized by the squared electron density). The emissivity model used here is provided by the latest version of the CHIANTI atomic database and plasma emission model (Del Zanna *et al.*, 2015; Landi *et al.*, 2013).

Due to unresolved coronal dynamics, tomographic reconstructions exhibit negative values of the reconstructed FBE, or zero when the solution is constrained to positive values (Frazin, 2000; Frazin, Vásquez, and Kamalabadi, 2009). These non-reconstructed voxels are indicated in black color in the latitude-longitude (Carrington) maps of DENT results in Section 3.

The cadence of the data time-series is set to 6 hr.

In this work the cadence of the data time-series was set to 6 hr and data from three EUV bands were used: 171, 193 and 211 Å in the case of AIA, and 171, 195 and 284 Å bands in the case of EUVI. When using data from three bands, a Gaussian model for the LDEM is able to accurately predict the tomographic emissivities (Frazin, Vásquez, and Kamalabadi, 2009; Nuevo *et al.*, 2015). In each tomographic voxel the problem is then reduced to finding the values of the three free parameters of the Gaussian (centroid, standard deviation, and area) that allow to best reproduce the three tomographically reconstructed values of FBE in that voxel.

Once the LDEM is determined at each voxel, the LDEM-averaged squared electron density  $N_m^2$  and electron temperature  $T_m$  in the voxel can be computed by taking its zeroth and first moments over temperature. More specifically, at the  $i$ -th voxel,

$$N_{m,i}^2 = \langle N_e^2 \rangle_i = \int dT \text{LDEM}_i(T), \quad (2)$$

$$T_{m,i} = \langle T_e \rangle_i = \frac{1}{\langle N_e^2 \rangle_i} \int dT T \text{LDEM}_i(T). \quad (3)$$

We define next a measure of the accuracy of the LDEM model to predict the tomographic FBEs in each voxel, as

$$R_i \equiv (1/K) \sum_{k=1}^K \left| 1 - \text{FBE}_{i,\text{syn}}^{(k)} / \text{FBE}_{i,\text{tom}}^{(k)} \right|, \quad (4)$$

being the average relative difference between the tomographic and the synthetic FBEs. The final product of DEMT is in the form of 3D maps of the LDEM-averaged quantities  $\sqrt{N_m^2}$  and  $T_m$ , as well as of the measure  $R$ .

## 2.2. AWSoM Simulations

AWSoM addresses coronal heating by including the non-linear interaction of forward propagating and counter-propagating (reflected) Alfvén waves which results in a turbulent cascade. The model accounts for anisotropic (parallel and perpendicular) proton temperatures and isotropic electron temperature. The dissipated turbulent energy is distributed over these three temperatures based on the theories of linear wave damping and stochastic heating. AWSoM does not use ad-hoc heating functions and accounts for both collisional and collision-less electron heat conduction. The Alfvén wave number associated with the damping rate is determined by the critical balance condition which uses the cascade time of the minor wave (Lithwick, Goldreich, and Sridhar, 2007) instead of the previously used cascade time of the major wave (Chandran *et al.*, 2011; van der Holst *et al.*, 2014). This energy partitioning, in the improved version of AWSoM, leads to more electron heating and less solar wind acceleration. To solve anisotropic MHD equations with radiative cooling, heat conduction and wave turbulence, AWSoM uses the Block-Adaptive-Tree-Solarwind-Roe-Upwind Scheme (BATS-R-US, Powell *et al.*, 1999; Tóth *et al.*, 2012) numerical scheme. MHD equations employed within the AWSoM model are detailed in van der Holst *et al.* (2014). Recently, Sachdeva *et al.* (2019) validated the AWSoM simulation results with a suite of observations from near the Sun upto 1 AU for solar minimum conditions.

Global maps of the observed photospheric magnetic field are essential for accurate modeling of the solar corona and are the primary input for AWSoM. The model use GONG synoptic map as input for CR-2082 (2009-04-05 - 2009-05-03) and ADAPT-GONG global magnetic field map for CR-2208 (2018-09-02 to 2018-09-29). ADAPT-GONG maps are unavailable for CR-2082. GONG provides synoptic full disk line-of-sight surface map of the radial magnetic field component. The unobserved polar fields in GONG are estimated by fitting a polynomial to neighboring observed fields. An improvement over these maps is provided by the ADAPT model (Worden and Harvey, 2000) which creates synchronic-synoptic maps that uses supergranulation, meridional circulation, flux-transport and differential rotation to evolve the magnetic field on the Sun for better estimates of the unobserved photospheric field (Arge *et al.*, 2010; Henney *et al.*, 2012). In AWSoM, the 2D radial photospheric field is converted to 3D magnetic field using the PFSS model which specifies the initial condition. We take the source surface to be at  $2.5 R_\odot$  and the magnetic field is radial at this height. The radial component specifies the boundary condition. Based on Chandran *et al.* (2011) the stochastic heating exponent is taken to be 0.21 and amplitude is 0.18 to account for energy partitioning between electrons and

protons. The Alfvén wave energy boundary condition is given by the poynting flux ( $S_A$ ) of the outgoing wave  $(\frac{S_A}{B})_\odot = 1.0 \times 10^6 \text{ Wm}^{-2}\text{T}^{-1}$  and the correlation length of the Alfvén waves is set to,  $L_\perp \sqrt{B} = 1.5 \times 10^5 \text{ m}\sqrt{T}$ .

The base of the transition region (TR) forms the inner boundary of the model (at  $\approx 1.0 R_\odot$ ). To ensure that the base of the TR is not affected by chromospheric evaporation we overestimate the density at the inner boundary,  $N_e = N_i = N_\odot = 2 \times 10^{17} \text{ m}^{-3}$  corresponding to the isotropic temperature values,  $T_e = T_i = T_{i\parallel} = T_\odot = 50,000 \text{ K}$ . The upper chromosphere is required to extend radially for the density to fall rapidly to correct (lower) values (Lionello, Linker, and Mikić, 2009). In reality, the thin transition has steep gradients in temperature and density as a result of the balance between coronal heating, heat conduction and the radiative losses. To resolve these gradients excessive numerical resources are required. As described in Lionello, Linker, and Mikić (2009); Sokolov *et al.* (2013) we artificially broaden the transition region to resolve with our finest grid resolution of  $\approx 0.001 R_\odot$ . This results in pushing the corona outwards. At this level, the radiative losses are sufficiently low so that the temperature can increase monotonically with height and form the transition region. Consequently, AWSoM results below  $\approx 1.05 R_\odot$  were not taken into account in this article.

The computational domain for solar corona extends from 1 to 24  $R_\odot$ . The spherical grid is radially stretched (with a maximum resolution of  $0.001 R_\odot$  near the Sun) with the z-axis aligned with the rotation axis in Heliographic Rotation coordinates. The Adaptive Mesh Refinement resolves the angular size to  $1.4^\circ$  between  $1 - 1.7 R_\odot$  and  $2.8 R_\odot$  outside. The solar corona component uses about 3 million cells on a  $6 \times 8 \times 8$  grid block. Local time stepping is used to speed up the steady state convergence. AWSoM simulation results provide the 3D distribution of density and temperature in addition to the 3D magnetic structure and velocity of the solar wind.

### 2.3. Tracing Results Along Magnetic Fieldlines

To determine the electron density and temperature along individual magnetic field lines, first both the thermodynamic results and the magnetic field obtained with the AWSoM model were interpolated into the DGMT grid. Then, the geometry of the field lines is determined by numerical integration of the first order differential equations  $dr/B_r = r d\theta/B_\theta = r \sin(\theta) d\phi/B_\phi$ , both inwards and outwards, from the specified 3D coordinates of a starting point. In order to evenly sample the whole volume spanned by the DGMT reconstructions, one starting point is selected at the center of each tomographic cell at 6 uniformly spaced heights, ranging from  $1.025$  to  $1.225 R_\odot$ , and every  $2^\circ$  in both latitude and longitude, for a total of 96,000 starting points.

For analysis purposes, the traced magnetic field lines are classified as open or closed according to their full geometry. Each closed field line is further classified as “small” or “large”, according to its coronal length  $L$  being respectively smaller or larger than the median value of the whole population, which is  $\text{Md}(L) \approx 0.5 R_\odot$  for both rotations. Finally, each closed magnetic field line is separated in

its two “legs”, defined as the two segments that go from each of its two footpoints (i.e. their location at  $r = 1 R_\odot$ ) to its apex (i.e., the location of maximum height).

At this stage, DENT and AWSOM products can be traced along open and closed magnetic field lines. Once the field line geometry is computed in high spatial resolution, only one sample point per tomographic cell is kept (the median one). To each sample point, the results corresponding to the tomographic voxel where it is located are assigned to it. As a result, for each field line one data point per tomographic cell is obtained. This approach was firstly used by Huang *et al.* (2012) to study temperature structures in the solar minimum corona and by Nuevo *et al.* (2013) to expand that analysis to rotations with different level of activity.

For each open field line and for each closed field leg, an exponential fit was applied to the electron density data points and a linear fit applied to the electron temperature data points. For the DENT model the data points used were  $\sqrt{N_m^2(r)}$  and  $T_m(r)$ , and in case of the AWSOM models the data points used were  $N_e(r)$  and  $T_e(r)$ . The exponential and linear fit equations are described by

$$\sqrt{N_m^2} = N_0 \exp[-(h/\lambda_N) / (r/R_\odot)] \quad (5)$$

$$T_m = T_0 + m h \quad (6)$$

where  $h \equiv r - 1 R_\odot$  is the coronal height measured from the photosphere. In the electron density fit,  $\lambda_N [R_\odot]$  is the density scale height and  $N_0 [\text{cm}^{-3}]$  is the electron density at the footpoint ( $h = 0$ ) of the loop. In the electron temperature fit,  $m [\text{MK}/R_\odot]$  is the slope and  $T_0 [\text{MK}]$  is the electron temperature at the footpoint of the loop. The slope  $m$  is the radial gradient of the electron temperature along the loop, which we denote as  $m = \nabla_r T_m$  hereafter, being  $\nabla_r \equiv \mathbf{e}_r \cdot \nabla$  the radial derivative operator, where  $\mathbf{e}_r$  is the heliocentric radial unit vector.

In the case of the electron density, the fitted function corresponds to the isothermal hydrostatic equilibrium solution, allowing for variation of the solar gravitational acceleration with height. This choice of function provides a straightforward means to directly evaluate how compatible is the observed coronal thermodynamical state with the hydrostatic solution.

Coronal magnetic structures for which temperature increases/decreases with height (in the inner corona) were dubbed as “up”/“down” loops by Huang *et al.* (2012) and Nuevo *et al.* (2013), who first reported their presence by means of DENT studies. As speculated by the authors of those works, loops of type down can be expected if the heating deposition is strongly confined near the coronal base of a magnetic loop. Down loops were first predicted by Serio *et al.* (1981), and later on by Aschwanden and Schrijver (2002). In a recent study, Schiff and Cranmer (2016) reproduced both down and up loops by means of numerical simulations, using a 1D steady-state model and considering time-averaged heating rates.

To determine if the leg of a traced field line is of type up or down, we first determine the Pearson correlation coefficient  $\rho(T, r)$  between the DENT temperature  $T_m$  and the heliocentric height  $r$  data points. We then select field lines for which the temperature is significantly correlated with height by requiring



$|\rho(T, r)| > 0.5$ . To test the goodness of the fit to the temperature-height data we perform a chi-squared test (Press *et al.*, 2002) considering the uncertainty of the DENT data points, selecting legs for which the fit matches the data with a 90% confidence level. In this way, legs for which the DENT temperature does not show a significant correlation with height, or the linear fit to temperature is not good enough, are excluded from the analysis. The test is also applied to the density-height data points, to ensure the trend is reasonably represented by the exponential fit. Finally, selected legs are then classified as up or down according to if  $\nabla_r T_m > 0$  or  $\nabla_r T_m < 0$ , respectively. The linear fit allows characterization of the variation of  $T_m$  with height by means of a characteristic temperature gradient  $\nabla_r T_m$  [MK/R<sub>⊙</sub>] along each leg. The chi-squared test to evaluate the quality of the fits considers the uncertainty level in the DENT products due to systematic sources (radiometric calibration and tomographic regularization), that Lloveras *et al.* (2017) estimated to be  $\Delta T_m \approx 10\%$  and  $\Delta \sqrt{N_m^2} \approx 5\%$ . In summary, to be selected a leg must meet all three following conditions:

- i) The leg must go through at least five tomographic grid cells with reconstructed data, and there must be at least one data point in each third of the range of heights spanned by the leg. This requirement is set to ensure a reasonably spread sample of heights along the leg.
- ii) The DENT temperature and height data points must meet  $|\rho(T, r)| > 0.5$ .
- iii) The confidence level of both the exponential and linear fits must be larger than 90%.

To characterize the global thermodynamic state of the inner solar corona in distinct magnetic structures, the DENT and AWSOM results were traced along the magnetic field lines of the latter model. Based on the geometry and size of the loops, as well as on their thermodynamical properties, their legs were classified in four different types in this work:

- Type 0: closed-small-down with footpoints in the range  $|\text{latitude}| < 50^\circ$ .
- Type I: closed-small-up with footpoints in the range  $|\text{latitude}| < 50^\circ$ .
- Type II: closed-large-up with footpoints in the range  $|\text{latitude}| > 40^\circ$ .
- Type III: open with footpoint in the range  $|\text{latitude}| > 60^\circ$ .

Legs of type down turn out to have a significant population only for closed-small loops. In the case of closed-large loops and open field lines, there are very few cases of type down. Hence, the requirement of being up for legs of type II and III is included above to select the vastly dominating population in each case. In Section 3, the results of both the DENT and AWSOM models in the distinct magnetic structures are statistically analysed. As shown in Section 3.1, classification of legs from type 0 through II allows studying the streamer belt in three distinct, progressively outer layers.

## 2.4. Energy Input Flux

The high temperature of the corona requires heating mechanisms to compensate for the the losses. While the vast majority of the existing literature on coronal

heating focuses on ARs, some studies have been dedicated to the heating of quiet-Sun regions. In particular, Mac Cormack *et al.* (2017) developed a new application of the DENT technique to estimate the energy input flux required at the base of quiet-Sun coronal loops to maintain them stable. The technique is based on tracing the DENT results along field lines of a global coronal magnetic model, just as described in the previous Section 2.3.

Consider a simple energy balance for each magnetic flux tube, in which the dominating losses of radiative power ( $E_r$ ) and thermal conduction power ( $E_c$ ) are compensated by a coronal heating power ( $E_h$ ) (Aschwanden, 2004):

$$E_h(s) = E_r(s) + E_c(s), \quad (7)$$

where  $s$  is the position along the flux tube and the power quantities are in units of  $[\text{erg sec}^{-1} \text{ cm}^{-3}]$ .

The thermal conduction power  $E_c$  equals the divergence of the conductive heat flux  $F_c$ , i.e.  $E_c(s) = [1/A(s)] d[A(s) F_c(s)]/ds$ , where  $A(s)$  is the transversal area of the magnetic flux tube at position  $s$ . Under a quiescent solar corona plasma regime, the conductive flux is assumed to be dominated by the electron thermal conduction, described by the usual Spitzer model (Spitzer, 1962)

$$F_c(s) = -\kappa_0 T(s)^{5/2} \frac{dT}{ds}(s), \quad (8)$$

where  $\kappa_0 = 9.2 \times 10^{-7} \text{ erg sec}^{-1} \text{ K}^{-7/2}$  is the Spitzer thermal conductivity.

Radiative power depends on the amount of plasma in certain temperatures that can radiate. The model estimate it by integrating the squared density multiplied by a radiative loss function  $\Lambda(T)$ . This function depends on plasma temperature and is calculated by the atomic database and the plasma emission model from CHIANTI (Del Zanna *et al.*, 2015). Then, the expression for radiative power obtained is:

$$E_r = \int dT \text{ LDEM}(T) \Lambda(T) \quad (9)$$

The energy balance given by Equation 7 is then integrated in the volume of any given coronal magnetic flux tube. Dividing the result by the flux tube area at the coronal base, and making use of the soleidonal condition of the magnetic field, a field-line integrated version of that energy balance is found,

$$\phi_h = \phi_r + \phi_c, \quad (10)$$

where the line integrated flux quantities  $\phi_{r,c} [\text{erg sec}^{-1} \text{ cm}^{-2}]$  are given by (Mac Cormack *et al.*, 2017),

$$\phi_r = \left( \frac{B_0 B_L}{B_0 + B_L} \right) \int_0^L ds \frac{E_r(s)}{B(s)} \quad (11)$$

$$\phi_c = \left( \frac{B_0 F_{c,L} - B_L F_{c,0}}{B_0 + B_L} \right) \quad (12)$$

Note that, for any given field line, all quantities in these two expressions can be computed from DENT model through Equations 8-9. Once computed, the quantity  $\phi_h$  can be calculated, which is the energy input flux required at the coronal base of each coronal field-line to maintain a stable coronal structure.

### 3. Results

#### 3.1. Tomographic Results

As described in Section 2.1, we carried out DENT reconstructions of the coronal structure for target rotations CR-2082 and CR-2208 using STEREO/EUVI and SDO/AIA data, respectively. Once the LDEM was determined for each rotation, the square root of the mean value of the electron density squared ( $\sqrt{N_m^2}$ ) and the electron mean temperature ( $T_m$ ) were computed at each voxel of the tomographic computational grid by means of Equations 2 and 3, and the measure  $R$  was calculated by means of Equation 4.

As an example, Figures 1 and 2 show latitude-longitude maps of DENT results for both rotations. Three different heights of interest are selected from the tomographic grid, providing also a detailed 3D view of the tomographic results: the lowest height of the tomographic grid ( $1.025 R_\odot$ ), the lowest height where the AWSOM results are fully consistent with coronal conditions ( $1.065 R_\odot$ ), and a middle height of the tomographic grid ( $1.105 R_\odot$ ). Black voxels correspond to non-reconstructed voxels (see Section 2.1). Thick-black curves indicate the open/closed boundaries of the magnetic field of the AWSOM model.

Both target rotations are highly axisymmetric, i.e. characterized by a high azimuthal symmetry. Rotation CR-2082 showed two small active regions (ARs), both near latitude  $+30^\circ$  and around longitudes  $50^\circ$  and  $120^\circ$ , respectively. Rotation CR-2208 showed two ARs, both near latitude  $+5^\circ$  and around longitudes  $140^\circ$  and  $300^\circ$ , respectively.

The magnetically open and closed regions of the AWSOM model are associated to Coronal holes (CHs) and the equatorial streamer belt, respectively. Consistently with that, the location of the open/closed boundaries derived from the respective AWSOM model quite accurately matches the regions of the DENT maps which exhibit the strongest latitudinal gradient of both the electron density and temperature.

Figures 1 and 2 show that the DENT reconstruction of the streamer belt is characterized by relatively larger values of density and temperature in comparison to the CHs. They also show that the streamer belt region of CR-2082 was denser and colder than that of CR-2208. In the case of CR-2082, which belongs to the deep minimum epoch between SCs 24 and 25, the low latitudes of the streamer belt are characterized by lower electron temperature than in its mid-latitudes. A similar behavior is seen in CR-2208, belonging to the declining phase

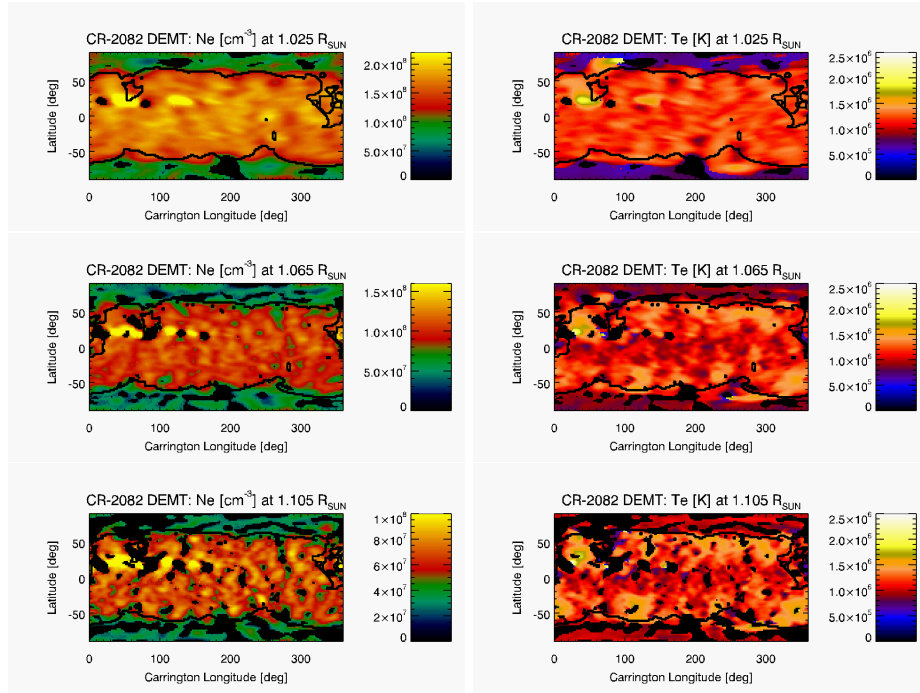


**Figure 1.** Carrington maps of DMT products  $\sqrt{N_m^2}$  (left panels) and  $T_m$  (right panels) for CR-2082. Top, middle and bottom panels show the results at three heliocentric heights, 1.025, 1.065 and 1.105  $R_\odot$  respectively. Black voxels correspond to non-reconstructed regions (see text in Section 3.1) and thick-black curves indicate the open/closed boundaries.

of SC 25, but having a somewhat less axisymmetric structure this characteristic is not so obvious. This thermodynamic structure of the streamer have been reported for other solar minimum rotations in previous DMT works (Lloveras *et al.*, 2017; Nuevo *et al.*, 2013; Vásquez, Frazin, and Manchester, 2010).

For both target rotations, Figure 3 shows latitude-longitude maps of the DMT measure  $R$  defined by Equation 4, at the same three heights shown in Figures 2 and 3. In most of the coronal volume of the DMT grid the agreement between the tomographic and synthetic FBEs is  $\lesssim 1\%$ . The notable exception is to be found in the CHs of the target rotation analysed based on AIA data. A similar results was found in the two existing DMT works based on data provided by the AIA instrument (Nuevo *et al.*, 2015; Mac Cormack *et al.*, 2017). This point is further discussed below.

Figure 1 shows the ADAPT-GONG and GONG global maps for CR2208. The two maps show significant differences, especially in the polar regions. We find that using ADAPT-GONG maps as input to the AWSoM model produces significantly better results in comparison to using GONG maps. Therefore, in this work we use ADAPT-GONG global magnetic maps for both CR2208 and CR

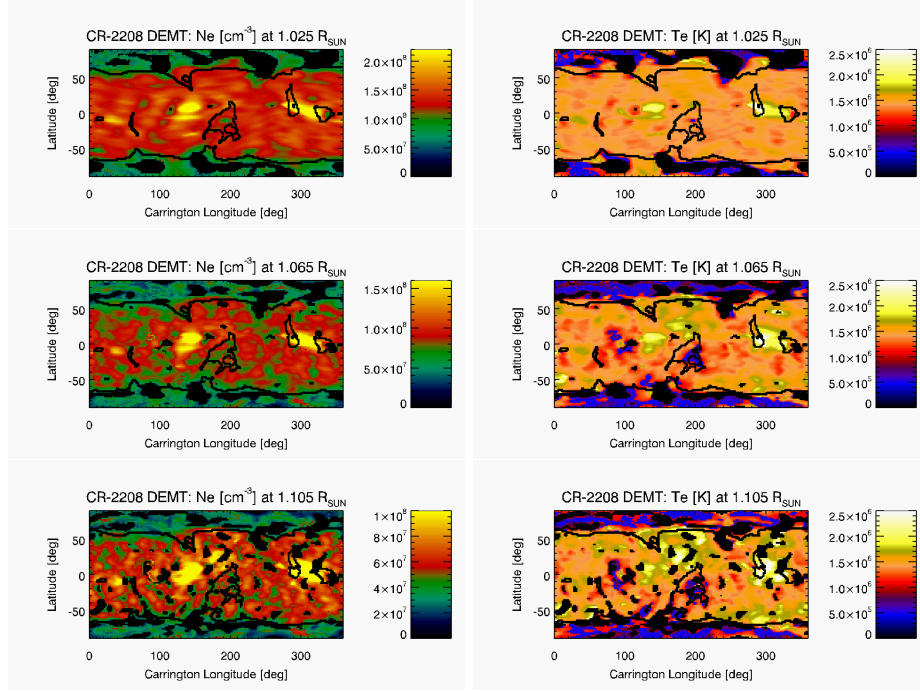


**Figure 2.** Same as Figure 1 but for CR-2208.

Figure 4 shows carrington maps of radial magnetic field ( $Br$ ) for both rotations at  $1.005 R_{\odot}$ . Both maps show a clear dipole. The main difference is observed in the polar region and is due to the different types of approaches that use GONG (CR-2082) and ADAPT-GONG (CR-2208.)

To characterize the DEMT results in different magnetic structures, we traced  $\sqrt{N_m^2}$  and  $T_m$  along the magnetic field lines of the AWSoM model. For both rotations, all legs that meet the criteria listed in Section 2.3 were selected. For each leg, the data points of electron density and electron mean temperature as a function of height were fitted to the Equations 5 and 6. As a result, the electron density  $N_0(r = 1.0 R_{\odot})$  and scale height  $\lambda_N$  were computed for each leg, as well as the temperature gradient  $\nabla_r T_m$ , and the height-averaged (along the leg) electron temperature  $\langle T_m \rangle$ .

For both target rotations, the top panels of Figure 5 show the latitude-longitude location (at heliocentric height  $r = 1.105 R_{\odot}$ ) of all traced field line legs for which criterion (i) of Section 2.3 is met. Open legs are indicated in gray color and closed ones in black color. For each leg, the fits to tomographic temperature and density were applied, as given by Equations 5-6. Considering the DEMT data points and the resulting fits along each leg, the bottom panels of Figure 5 show the latitude-longitude location of the subset for which also both criteria (ii) and (iii) of Section 2.3 are met. Using a four-color code, type 0, I, II and III legs are shown in blue, red, magenta and cyan color, respectively. Of the  $\approx 44000$  legs selected for CR-2082, 20% are type 0, 31% are type I, 23% are

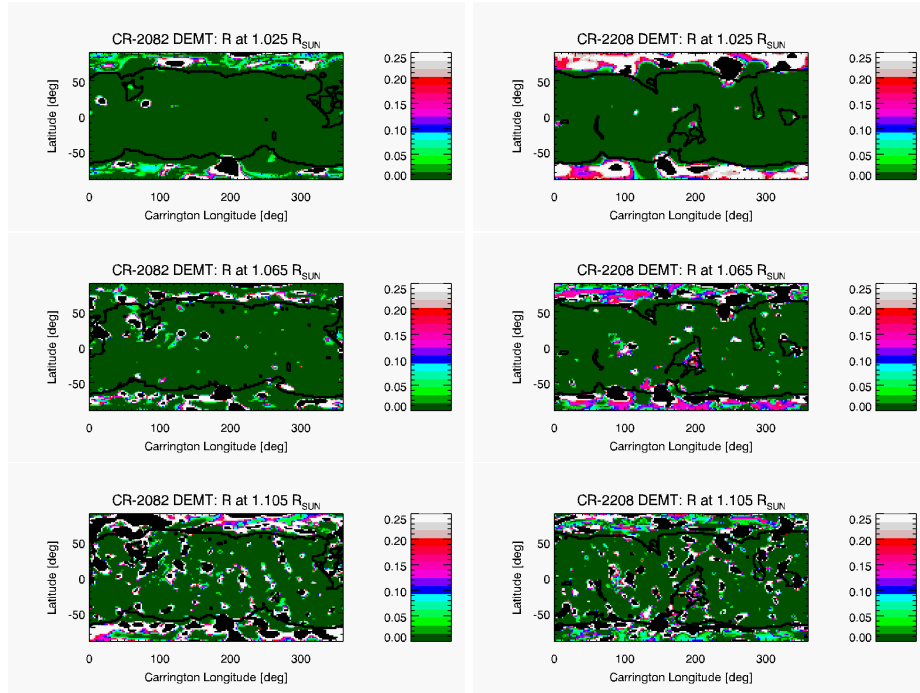


**Figure 3.** Carrington maps of the measure  $R$  defined by Equation 4, for CR-2082 (left panels) and CR-2208 (right panels), at heights 1.025, 1.065 and 1.105  $R_{\odot}$ , from top to bottom.

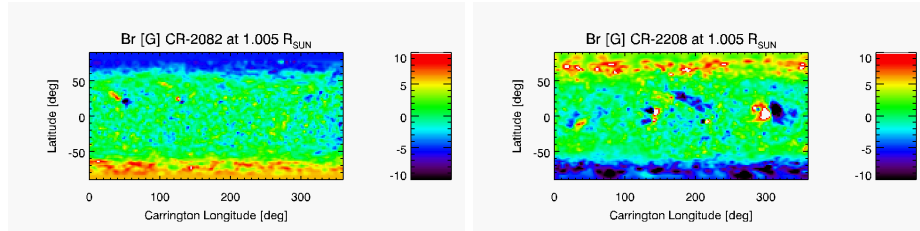


**Figure 4.** Carrington maps of radial magnetic field obtained with AWSoM at 1.005  $R_{\odot}$  for CR-2082 (left) and CR-2208 (right).

type II and 26% type III. On the other hand, of the  $\approx 44000$  legs selected for CR-2208, 10% are type 0, 43% are type I, 30% are type II and 17% type III.

Type 0 (small down) legs mainly populate the equatorial latitudes. This kind of structure was originally found by Huang *et al.* (2012), and their existence was shown to be anti-correlated with the solar activity level around the solar minimum between SCs 24 and 25 by Nuevo *et al.* (2013). Later on, Lloveras *et al.* (2017) showed that equatorial down loops in streamers were also to be found in the deep minimum between SCs 23 and 24. Here, we verify the existence of this type of structure for the two target rotations. The relatively smaller

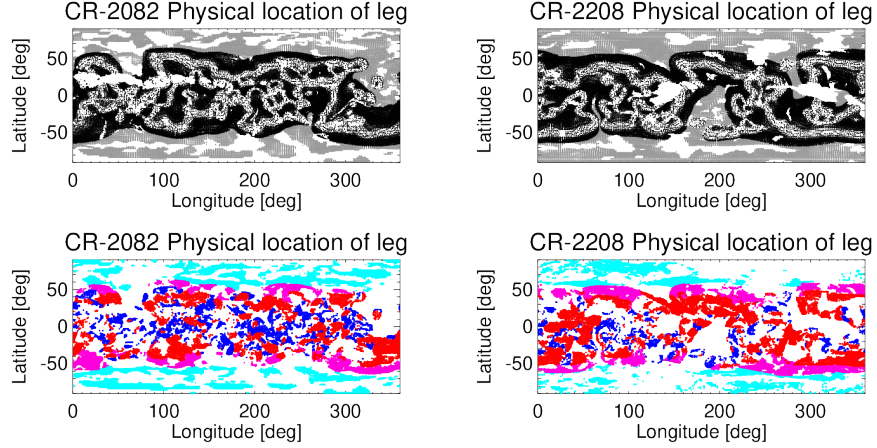


**Figure 5.** *Top panels:* latitude-longitude location at heliocentric height  $r = 1.105 R_{\odot}$  of all open (grey color) and closed (black color) traced field line legs for which criterion (i) of Section 2.3 is met, for both CR-2082 (left) and CR-2208 (right). *Bottom panels:* latitude-longitude location of the subset for which also both criteria (ii) and (iii) of Section 2.3 are met. The location of type 0, I, II and III legs is shown in blue, red, magenta and cyan color, respectively.

population of down legs seen in CR-2208, as compared to CR-2082, is consistent with the aforementioned results by Nuevo *et al.* (2013). Type I (small up) mainly populate the mid-latitudes, while type II (large up) legs are mostly very large trans-equatorial field lines forming the envelope of the streamer belt. Finally, type III (open) legs populate the CHs.

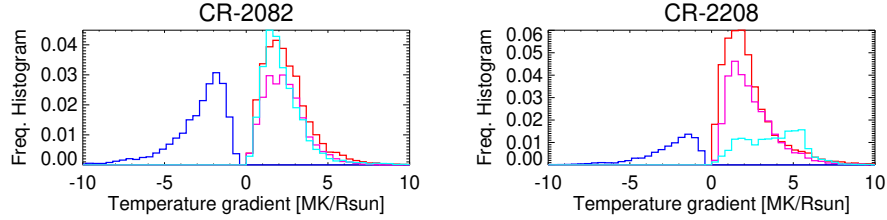


**Figure 6.** Frequency histograms of the temperature radial gradient for the four types of legs in Figure 5 (using the same color code) for CR-2082 (left panel) and CR-2208 (right panel).

Figure 6 shows frequency histograms of  $\nabla_r T_m$  for legs of type 0, I, II and III. The lack of population around values close to zero is due to the requirement  $|\rho(T, r)| > 0.5$  which discards quasi-isothermal legs. For both rotations, the median value of the temperature radial gradient is  $\text{Md}(\nabla_r T_m) \approx -2.5, +2.3$  and  $+2.4 \text{ MK/R}_{\odot}$  for legs of type 0, I and II, respectively.

The notable difference between both rotations is the characteristic value  $\text{Md}(\nabla_r T_m) \approx +4.5 \text{ MK/R}_{\odot}$  for legs of type III for CR-2208. This is related to the much larger  $R$  score for the DMT results along CH legs for CR-2208. In this case, DMT performs poorly in modeling a LDEM that predicts the

tomographic FBEs with reasonable accuracy. Indeed, visual inspection of the DENT temperature maps for CR-2208 in Figure 3, reveals that in most of the CH region the result for  $T_m$  below height  $1.105 R_\odot$  is quite uniform and artificially low. As it turns out, around and above height this height the score  $R$  is lower and the temperature results are more reliable. As a result, the temperature gradient along these legs is artificially larger, with the linear fit trying to simultaneously fit the artificially low values of  $T_m$  at lower heights. In general, the DENT results in the CH region based on AIA data are thus much less reliable than in the rest of the analysis. We will return to this point in the conclusion section.

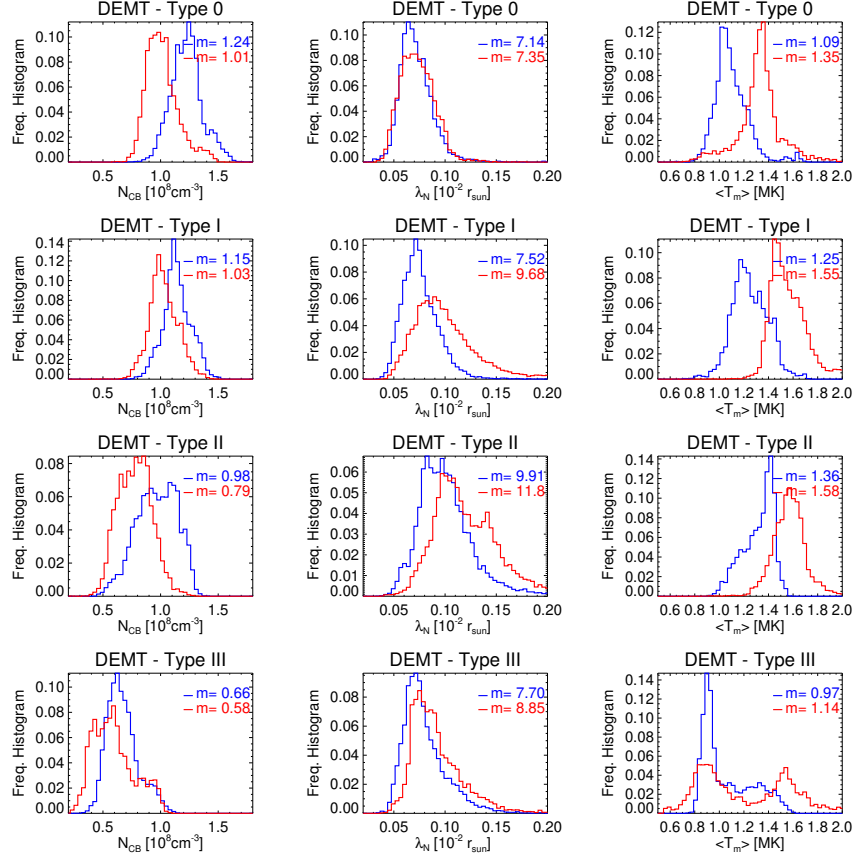


**Figure 7.** Statistical distribution of DENT results for rotations CR-2082 (blue) and CR-2208 (red) traced along legs of type 0, I, II and III (from top to bottom), as defined in Section 2.3. From left to right: electron density  $N_{CB} \equiv \sqrt{N_m^2}(r = 1.055 R_\odot)$ , electron density scale height  $\lambda_N$ , and loop-averaged temperature  $\langle T_m \rangle$ . In each panel the median value  $m$  is indicated.

For both rotations, Figure 7 shows, in a statistical fashion, the DENT results traced along field lines discriminated by leg type. From top to bottom results are shown for type 0 to type III legs, respectively. From left to right the panels show the statistical distribution of  $N_{CB} \equiv \sqrt{N_m^2}(r = 1.055)$  (the lowest height



where the AWSOM results are consistent with coronal conditions),  $\lambda_N$  and  $\langle T_m \rangle$ , with the median value  $m$  indicated in each plot.

Table 1 summarizes a quantitative comparative analysis between the results of the two target rotations. For CR-2082 quantities are expressed as absolute values, while for CR-2208 they are informed as a percentual variation relative to the corresponding results for CR-2082. The following major results, both concerning the structure of each rotation individually as well as their comparison, can be drawn.

**Table 1.** Median value (indicated as “Md”) of the statistical distribution of  $N_{CB}$ ,  $\lambda_N$ , and  $\langle T_m \rangle$  for each coronal type of legs defined in Section 2.3. For CR-2082 values are expressed in absolute terms, while for CR-2208 they are informed as a percentual variation relative to the CR-2082 value.

Type	Md( $N_{CB}$ ) [ $10^8 \text{ cm}^{-3}$ ]	Md( $\lambda_N$ ) [ $10^{-2} \text{ R}_\odot$ ]	Md( $\langle T_m \rangle$ ) [MK]
0	1.24 (-19%)	7.1 (+ 3%)	1.09 (+24%)
I	1.15 (-10%)	7.5 (+29%)	1.25 (+24%)
II	0.98 (-20%)	9.9 (+19%)	1.36 (+16%)
III	0.66 (-12%)	7.7 (+15%)	0.97 (+18%)

Throughout the magnetically closed region of both rotations, type 0, I and II legs, associated to increasingly outer layers of the equatorial streamer belt, exhibit progressively decreasing coronal base density, increasing density scale height, and increasing electron temperature. In both rotations also, type III legs in the CHs are characterized by sub-MK temperatures, and electron density values of order  $\approx 1/2$  of those observed for the type 0 and type I legs in the core of the equatorial streamer.

A comparison of the results between the two rotations shows that, compared to CR-2082, target rotation CR-2208 was characterized by  $\approx 10 - 20\%$  lower values of the electron density at the coronal base,  $\approx 5 - 30\%$  larger values of density scale height, and  $\approx 5 - 25\%$  larger values of the electron temperature.

To analyze the loop-integrated energy flux quantities introduced in Section 2.3, we selected closed loops for which both legs have the same sign of the radial gradient of the electron temperature  $\nabla_r T_m$ . In this way, according to the classification of both its legs, each given loop was classified as of type 0 (small down loop), I (small up loop), or II (large up loop). For both target rotations, and for loops of type 0, I and II, Figure 8 shows the frequency histogram of the loop-integrated energy flux quantities  $\phi_r$ ,  $\phi_c$  and  $\phi_h$  in blue, green and red color, respectively.

For both rotations, the value of the loop-integrated radiative power  $E_r$ , measured by the quantity  $\phi_r$ , is largest for loops of type 0. This is due to  $E_r \propto N_e^2 \Lambda(T_e)$ , with both factors contributing to maximize  $E_r$  for loops of type 0. As shown in Figure 7 and Table 1, loops of type 0 are characterized by the largest values of electron density. Also, in the range of sensitivity of the EUVI and AIA

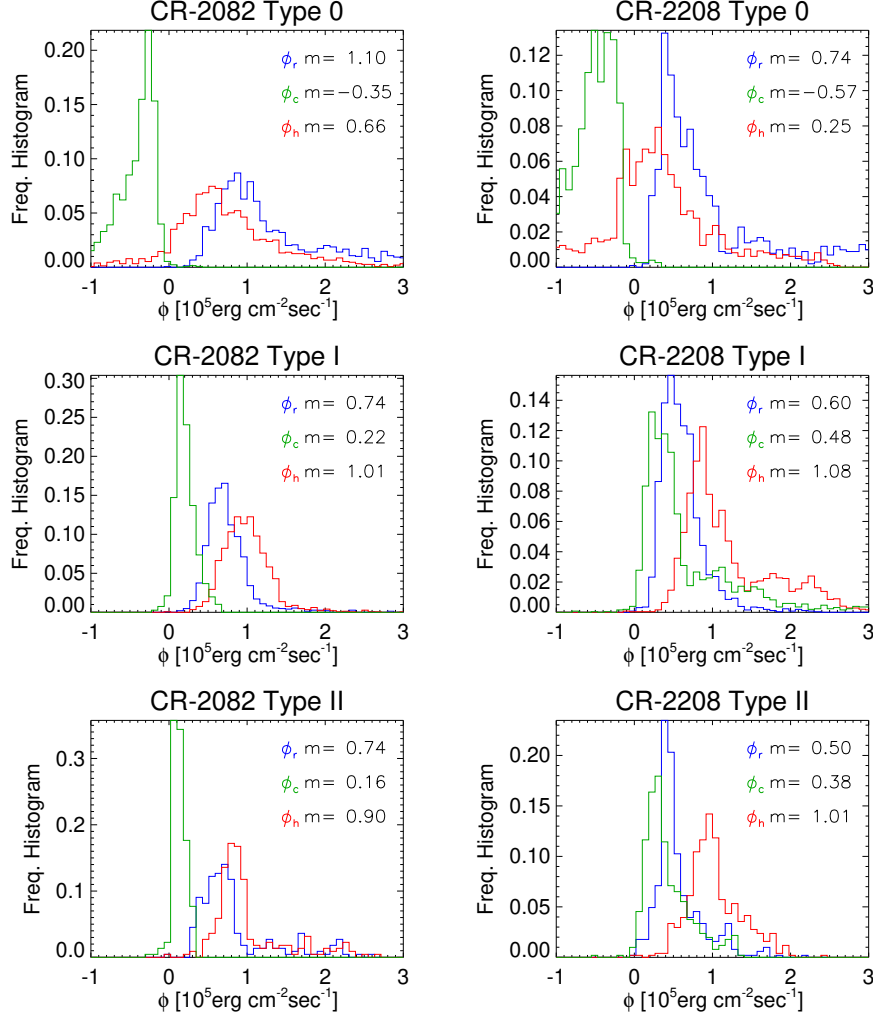


**Figure 8.** Statistical results of the loop-integrated energy flux quantities  $\phi_r$ ,  $\phi_c$ , and  $\phi_h$  in colors blue, red and green, respectively for CR-2082 (left) and CR-2208 (right). From top to bottom, panels show the results for loops of type 0, I and II, which are loops for which both legs meet the criteria from Section 2.3.

instruments, namely 0.5–3.0 MK (Nuevo *et al.*, 2015), the radiative loss function  $\Lambda(T)$  has a local maximum at  $T_c \approx 1$  MK. According to Figure 7, loops of type 0, I and II are characterized by values of temperature that are progressively larger and farther from the value  $T_c$ , for both rotations.

The sign of the quantity  $\phi_c$  depends on that of the conductive flux  $F_c$ . Equations 8 and 12 imply that down loops (type 0) and up loops (type I and II) are characterized by  $\phi_c < 0$  and  $\phi_c > 0$ , respectively, as verified in Figure 8.

Adding the radiative and conductive terms, the characteristic energy input flux at the coronal base is in the range  $\phi_h \approx 0.5 - 1.5 \times 10^5 \text{ erg cm}^{-2} \text{ s}^{-1}$ , depending on the rotation and the type of loop, matching the values reported by Mac Cormack *et al.* (2017). Note that for type 0 loops there is a marginal population characterized by the unphysical result  $\phi_h < 0$ . As shown by Mac Cormack *et al.* (2017), this affects only the smallest sized loops of the type 0, and it is most probably due to the limited temperature sensitivity of the instrumental passbands. The radiative loss term is here calculated based on plasma emission detected by three coronal bands of EUVI or AIA. Though accounting for most of the coronal plasma, there surely is additional emission out of the instrumental sensitivity range. As a result, the positive term  $\phi_r$  is most likely underestimated, leading to values  $\phi_h < 0$  in loops of type 0, being characterized by  $\phi_c < 0$ .

### 3.2. Comparison of the DMT and AWSoM Models

For both target rotations, Figures 9 and 10 show latitude-longitude maps of the AWSoM electron density and temperature. Maps are shown at the same three heights selected for visualization of the DMT results in Figures 1 and 2. Thick-black curves indicate the magnetic open/closed boundaries based on the magnetic field of the AWSoM model. Visual inspection of these maps shows that the AWSoM model for both rotations is highly axisymmetric, as the tomographic model.

As described in Section 2.2, the AWSoM model includes an artificially thick TR, achieving coronal conditions above height  $\approx 1.06 R_\odot$ . Indeed, the top panels in Figures 9 and 10, at height  $1.025 R_\odot$ , clearly do not represent coronal conditions (although we include them here for completeness). When compared to DMT results (Figures 1 and 2), the latitude-longitude maps of the AWSoM model for heights  $1.065$  and  $1.105 R_\odot$  capture well the denser and hotter equatorial streamer belt surrounded by the less dense and colder CHs. Furthermore, for both target rotations, the temperature maps show the low latitudes of the equatorial streamer belt to be characterized by lower temperatures than its mid-latitudes, as also seen in the DMT results. The latitude-longitude maps of the AWSoM and DMT results are shown in the same units and scales, so that a visual comparison among them already reveals similar values of electron density and temperature in both models.

Being highly axisymmetric target rotations, the longitude-averaged latitudinal variation of the results of both models is an informative way to compare their large-scale structure. Such comparison is shown in Figure 11 at height  $1.105 R_\odot$ , with top panels comparing electron density and mid panels electron temperature. **For completeness the variation of  $Br$  is added in the lower panels.** In these longitude-averaged profiles, longitudes containing ARs or low latitude CHs were excluded. In each panel the averaged latitudinal variation for the DMT model is shown in solid-line style, while the result for the AWSoM model is shown in dashed-linesyle. Left panels show the comparison for CR-2082 (in blue) and right panels for CR-2208 (in red). In each panel the vertical black lines denote the corresponding longitude-averaged latitude of the open-close boundary in both hemispheres.

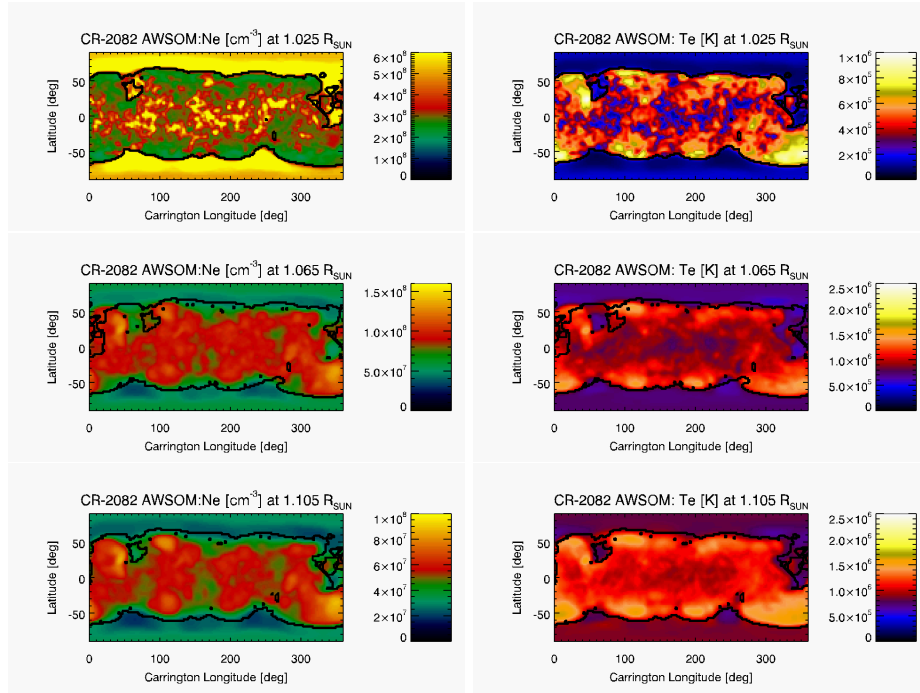


**Figure 9.** Carrington maps of density (left panels) and temperature (right panels) obtained with AWSOM model for the same three heights shown in Figure 1.

Several details from Figure 11 are worth being highlighted. Firstly, at most latitudes the overall agreement of the electron density of both models is within  $\approx 20\%$  for CR-2082, and  $\approx 5\%$  for CR-2208. The noticeable exception is to be found near the open/closed boundaries of both target rotations, where the disagreement between both models can be up to twice as much. In the case of the electron temperature, for both target rotations the models agree within  $\approx 15\%$  at all latitudes of the streamer belt, showing larger discrepancies in the CHs. Secondly, for both target rotations, and for both models, these plots clearly show the relatively lower temperatures characterising the low-latitudes of the equatorial streamer belt compared to its mid-latitudes. Thirdly, for both target rotations, the latitude of the open/closed magnetic boundary in both hemispheres matches the location of the strongest latitudinal gradient of the DMT electron density. Note this is not the case for the AWSOM model, that shows a minimum density at the open/closed boundary. Last, note that the DMT electron density decreases from the open/closed boundary towards the poles (in both hemispheres of the two target rotations), while the AWSOM model shows the opposite trend. **With regard to *Br*, it is worth pointing the plateau in the coronal hole region of CR-2082 and the decreasing tendency in the case of CR-2208.**

To characterize the results of the AWSOM model in distinct magnetic structures, its results for electron density and temperature were traced along its

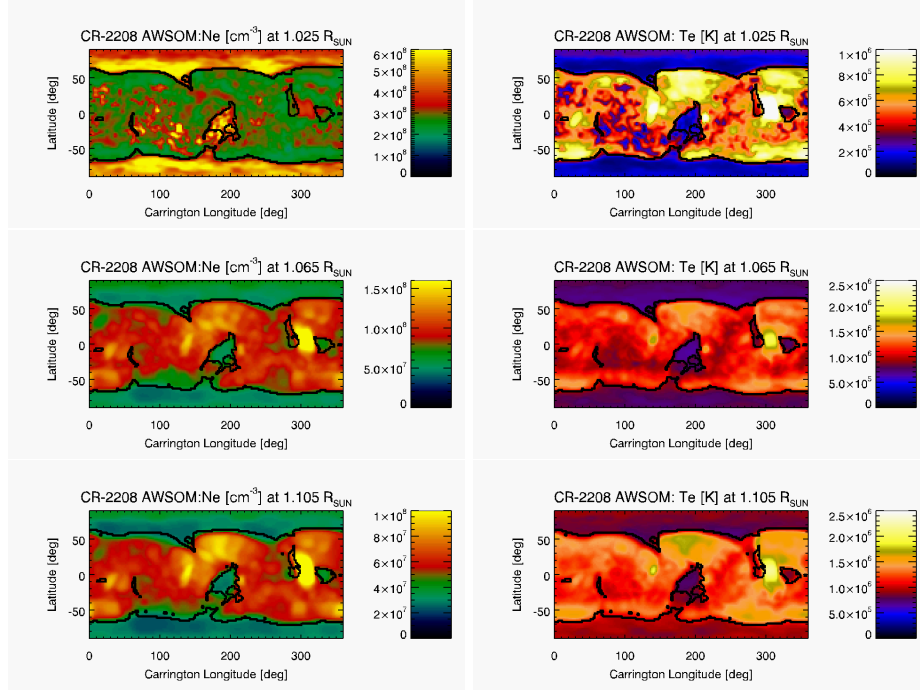


**Figure 10.** Same as Figure 10 for CR-2208.

magnetic field lines. For each field line leg, the results were then fit to Equations 5 and 6, considering only data points above heliocentric height  $1.055 R_{\odot}$ . We then classified the traced legs into types I, II and III, according to the criteria described in Section 2.3. Legs of type 0 are not included for AWSoM, as in its current implementation it can not simulate down loops, a point we will discuss in the next section.

For both target rotations, the top panels of Figure 12 show the latitude-longitude location (at heliocentric height  $1.105 R_{\odot}$ ) of all traced field line legs for which criterion (i) of Section 2.3 is met. That criterion is adapted here, requiring that at least five voxels of the tomographic grid are threaded by the leg. Open legs are indicated in gray color and closed ones in black color. For each leg, the fits to tomographic temperature and density were applied, as given by Equations 5 and 6. Considering the AWSoM data points and the resulting fits along each leg, the bottom panels of Figure 12 show the latitude-longitude location of the subset for which also both criteria (ii) and (iii) of Section 2.3 are met. Using a three-color code, type I, II and III legs are shown in red, magenta and cyan color, respectively. This figure is to be compared with the corresponding Figure 5 for DGMT results. It is readily seen that the AWSoM maps are more populated than those of DGMT. This is due to the 3D MHD model having electron density and temperature fields spatially smoother than those of DGMT.

For target rotation CR-2082, Figure 13 shows the statistical distribution of the results of the DGMT (solid line-style) and AWSoM (dashed line-style) models

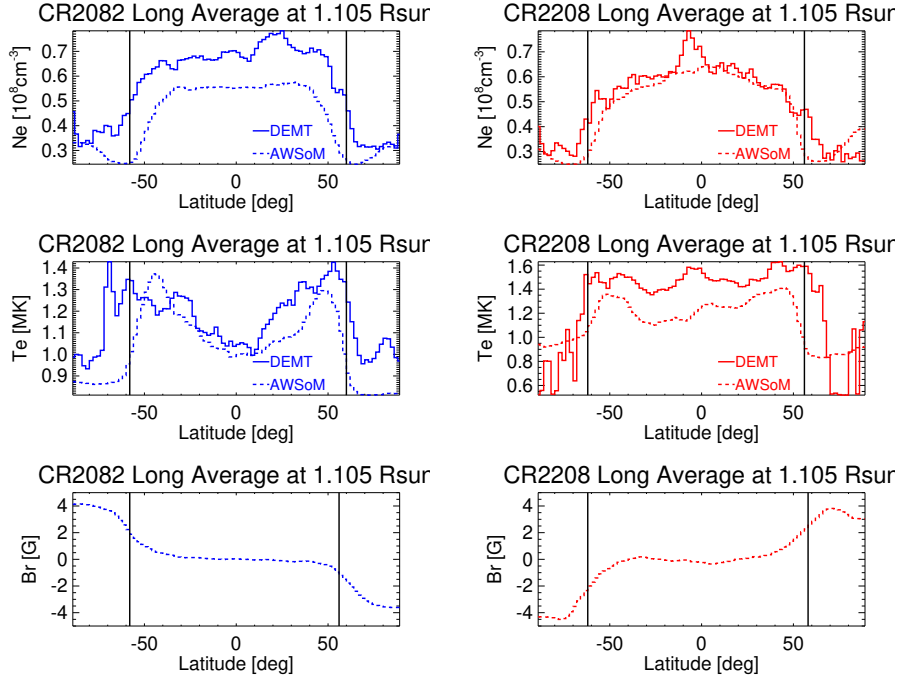


**Figure 11.** Longitude-averaged latitudinal dependence of the electron density (top) and temperature (bottom) for DEMT (blue) and AWSOM (red) results at  $1.105 R_{\odot}$ . The left (right) panels correspond to CR-2082 (CR-2208). The vertical black line indicates the longitude-averaged latitudes of the open/closed magnetic boundary in both hemispheres.

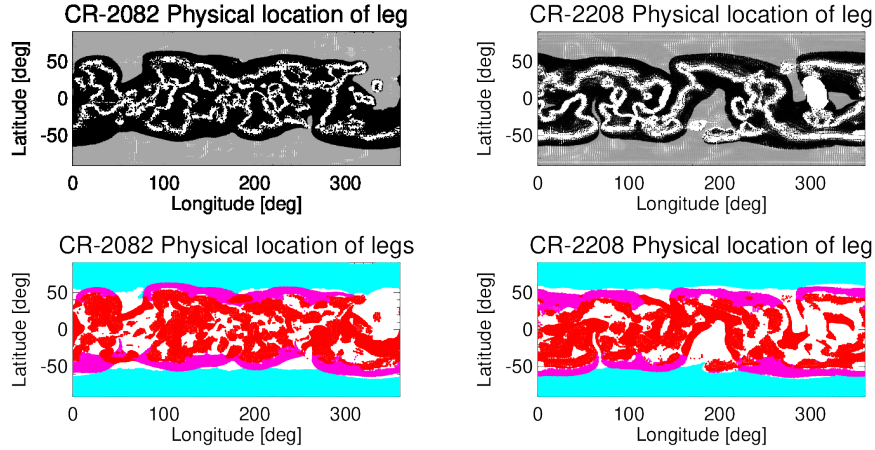


**Figure 12.** Same as Figure 5, but using the density and temperature of the AWSOM model to classify its legs in types I, II and III. The model does not exhibit legs of type 0.

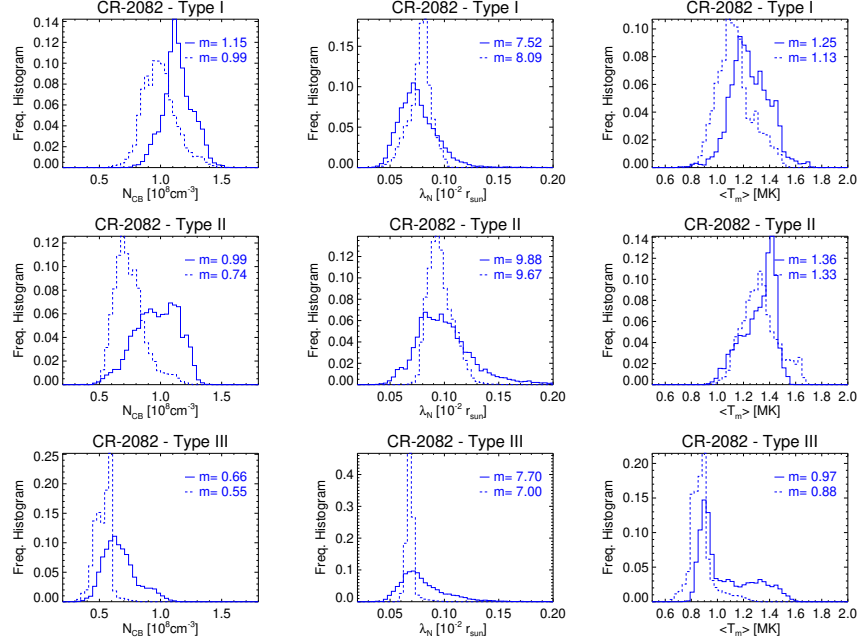


**Figure 13.** Statistical distribution of the results of the DMT (solid line-style) and AWSOM (dashed-line style) models traced along legs of type I, II and III (from top to bottom), as defined in Section 2.3. From left to right: electron density at the lowest coronal height of the AWSOM model  $N_{CB}(r = 1.055 R_{\odot})$ , electron density scale height  $\lambda_N$ , and leg-averaged electron temperature  $\langle T_m \rangle$ . In each panel the median values  $m$  are indicated.

traced along legs of type I, II and III (from top to bottom), as defined in Section 2.3. From left to right: electron density at the lowest coronal height of the AWSOM model  $N_{CB} \equiv N_e(r = 1.055 R_{\odot})$ , electron density scale height  $\lambda_N$ , and leg-averaged electron temperature  $\langle T_m \rangle$ . In each panel the median values  $m$  are indicated. Figure 14 shows the same analysis for target rotation CR-2208.

For the two target rotations, Table 2 summarizes a quantitative comparative analysis between the results of the DMT and AWSOM models based on the results shown in Figures 13 and 14. The DMT results are expressed as absolute values, while the AWSOM results are informed as a percentual variation relative to the corresponding result for DMT. The following major results can be drawn.

For target rotation CR-2082, the median value of the electron density  $N_{CB}$  of both models agree within  $\approx 10 - 25\%$ , depending of the type of leg, with the largest discrepancy found for legs of type II (near the open/closed boundary). The median value of the scale height  $\lambda_N$  agree within  $\approx 10\%$  in all regions. The leg-averaged electron temperature  $\langle T_m \rangle$  of both models also agree within  $10\%$  in all regions. For target rotation CR-2208 the agreement of the median value of  $N_{CB}$  and  $\lambda_N$  of both models is within  $10\%$ , while median values of  $\langle T_m \rangle$  agree within  $15\%$ . These detailed results, being consistent with the large-scale comparison provided in Figure 11, show in detail how the AWSOM model performs compared to DMT in different magnetic structures.

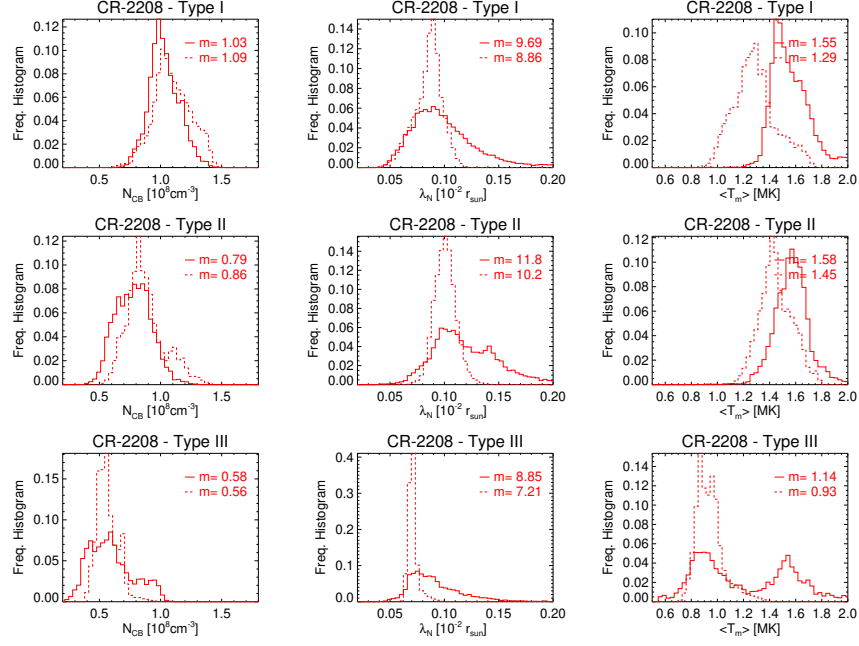


**Figure 14.** Same as Figure 13 for CR-2208.

Finally, to provide a graphical comparison of both models across the full range of heliocentric heights covered by the DEMT results, Figure 15 shows the average fits of  $N_e(r)$  and  $T_e(r)$  for legs of type I (red), II (magenta), and III (cyan) for

**Table 2.** Median value (indicated as “Md”) of the statistical distribution of  $N_{CB}$ ,  $\lambda_N$ , and  $\langle T_m \rangle$  for each coronal type of leg defined in Section 2.3. DEMT values are expressed in absolute terms, while AWSOM results are informed as a percentual variation relative to the corresponding DEMT value.

Type	Md( $N_{CB}$ ) [ $10^8 \text{ cm}^{-3}$ ]	Md( $\lambda_N$ ) [ $10^{-2} R_\odot$ ]	Md( $\langle T_m \rangle$ ) [MK]
CR-2082			
I	1.15 (−14%)	7.5 (+ 8%)	1.25 (−10%)
II	0.99 (−25%)	9.9 (− 2%)	1.36 (− 2%)
III	0.66 (−17%)	7.0 (− 9%)	0.97 (− 9%)
CR-2208			
I	1.03 (+ 6%)	9.7 (− 8%)	1.55 (−17%)
II	0.79 (+ 9%)	11.8 (−14%)	1.58 (− 8%)
III	0.58 (− 3%)	8.9 (−18%)	1.14 (−18%)



both target rotations. In each panel the DEMENT and AWSoM results are plotted in solid and dashed line styles, respectively.

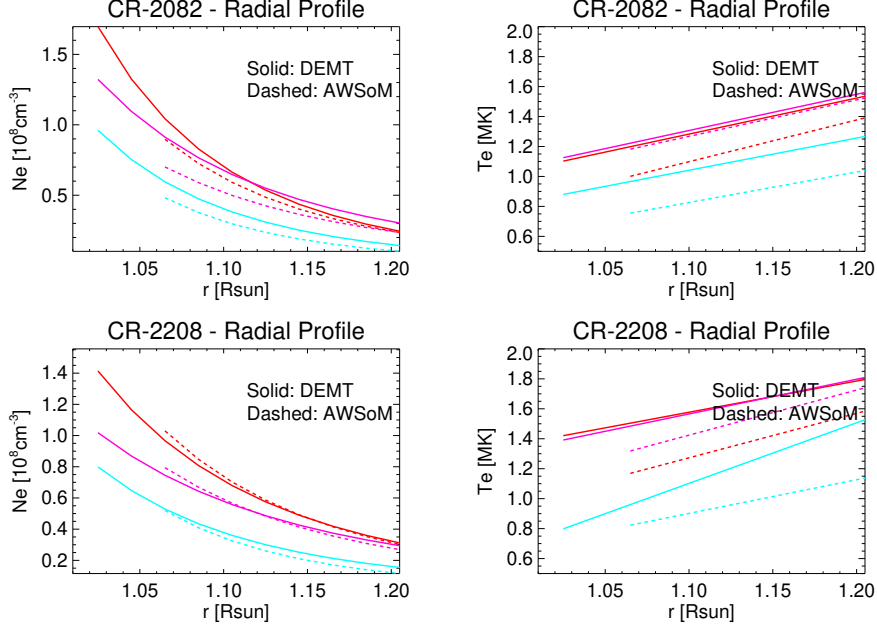


**Figure 15.** Average fits to  $N_e(r)$  (left panels) and  $T_e(r)$  (right panels) for legs of type I (red), II (magenta), and III (cyan), for CR-2082 (top panels) and CR-2208 (bottom panels). Solid lines correspond to DEMENT results while dashed lines correspond to AWSoM results.

As discussed above, Figure 11 shows that the longitude-averaged latitudinal profile of the DEMENT electron density in the CHs decreases towards the poles. Figure 16 below shows the longitude-averaged AWSoM radial wind speed  $V_r$  at  $6 R_{\odot}$ , where all field lines are open. The heliocentric current sheet (HCS) location is indicated by the minimum of the speed curve. For each rotation, all velocity data points to the south of the HCS position map down to the southern CH in Figures 11. Similarly, all velocity data points to the north of the HCS position map down to the northern CH in Figures 11. This clearly shows an anti-correlation between the DEMENT electron density at low heights and the AWSoM wind speed at larger heights.

#### 4. Discussion and Conclusions

We carried out the 3D DEMENT reconstruction and MHD modeling of the inner solar corona for two target rotations, CR-2082 and CR-2208. The first target belongs to the deep minimum epoch between SCs 23 and 24, while the latter belongs to the end of the declining phase of SC 24. The present work introduces two improvements in the implementation of DEMENT, namely the use of only off-limb data in the EUV images, and the inclusion of a 3D regularization scheme.

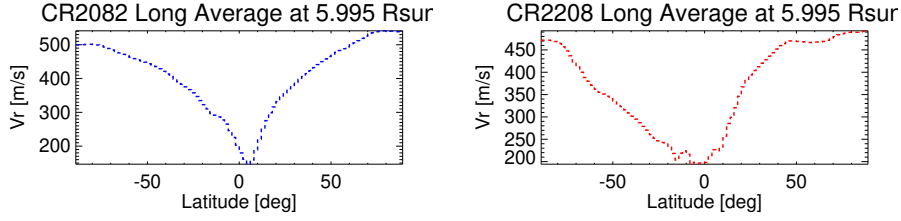


**Figure 16.** Longitude-averaged latitudinal dependence of the AWSoM model wind speed at  $6.0 R_{\odot}$  for CR-2082 (left panel) and CR-2208 (right panel).

As a result of the former, artifacts introduced by coronal dynamics are mitigated, and as a result of the latter, tomographic reconstructions behave more smoothly close to the radial boundaries of the computational grid when compared to previous reconstructions. The MHD model used is here the latest version of the AWSoM component of the SWMF suite.

Based on the magnetic field of AWSoM model and the results of the DENT model for electron density and temperature, we classified coronal structures in four different types. Smaller legs in the core of the streamer belt are classified in down/up types according to their temperature decreasing/increasing with height (dubbed type 0/I). Larger closed legs of type up that form the envelope of the streamer belt (dubbed type II), and open field lines of type up populating the CHs (dubbed type III).

Concerning the DENT reconstructions, Figure 5 shows that, for both target rotations, magnetic field lines of type 0, I and II are associated to increasingly outer layers of the equatorial streamer belt. Figure 7 and Table 1 report in 3D quantitative detail how these progressively outer magnetic structures exhibit progressively decreasing coronal base density, increasing density scale height, and increasing electron temperature. For both target rotations we find that down legs populate the low latitudes of the streamer belt, while up legs dominate its mid-latitudes. Also, in the case of CR-2082 the fraction of down legs is significantly larger than for CR-2208. These findings are consistent with previous studies by Huang *et al.* (2012) and Nuevo *et al.* (2013). In the case of the latter, they include in their analysis target CR-2081, which is a rotation almost identical to our target CR-2082. Our results for target CR-2082 compare very well with those of Nuevo *et al.* (2015) and Lloveras *et al.* (2017) for target CR-2081. As our study uses the improved version of the DENT technique, such comparison provided a consistency check for the changes implemented in the DENT technique.

For both target rotations, type III field lines in the CHs are characterized by sub-MK temperatures, and electron density values of order  $\approx 1/2$  of those observed for the type 0 and type I lines in the core of the equatorial streamer. In the case of the AIA based DENT reconstruction, we show that in a substantial fraction of the CHs region the technique performs poorly in modeling LDEMs that predict the tomographic emissivity in each EUV band with reasonable accuracy. As a result, DENT results based on AIA data are currently less reliable in the CH region. This was already found by the existing two previous DENT

works based on AIA data (Nuevo *et al.*, 2015; Mac Cormack *et al.*, 2017). The source of this distinct performance of DENT when applied to EUVI or AIA data is related to the TRFs of the respective filter sets. We are currently implementing an improved LDEM determination algorithm to deal with this issue that will be used in a follow up article.

In comparing the DENT results obtained for the two selected targets, we highlight here that they rely on data provided by two different instruments, namely EUVI and AIA for CR-2082 and CR-2208, respectively. In order to quantify the systematic difference of the DENT products based on both instruments, Nuevo *et al.* (2015), who were the first to apply DENT to AIA data, analysed a single target using both instruments independently. They found that while the density products are essentially equal, the temperature product of DENT based on AIA data is systematically 8% larger than the one based on EUVI data, i.e.  $T_m^{(\text{AIA})}/T_m^{(\text{EUVI})} \approx 1.08$ . Considering such correction, Figure 7 and Table 1 indicate that CR-2208 was characterized by temperatures  $\approx 10 - 15\%$  larger relative to CR-2082 throughout the streamer belt region. As for the electron density products, CR-2208 was found to be  $\approx 15 - 20\%$  less dense than CR-2082 throughout the streamer belt region. These systematic differences are around or beyond the uncertainty level in the DENT products due to systematic sources (radiometric calibration and tomographic regularization), that Lloveras *et al.* (2017) estimated to be  $\Delta T_m \approx 10\%$  and  $\Delta \sqrt{N_m^2} \approx 5\%$ .

In the streamer belt region we combined the DENT results and the AWSoM magnetic model to infer the energy input flux  $\phi_h$  at the coronal base required to maintain stable coronal loops. To this end, we applied the technique developed by Mac Cormack *et al.* (2017). We found characteristic values in the range  $\phi_h \approx 0.5 - 1.5 \times 10^5 \text{ erg cm}^{-2} \text{ s}^{-1}$ , depending on the rotation and the type of loop, matching the values reported by Mac Cormack *et al.* (2017). Based on spectroscopic data of the EIS instrument in quiet-Sun regions Hahn and Savin (2014) showed that, if the observed non-thermal broadening are assigned to Alfvén waves, their energy flux at the coronal base is estimated to be in the range  $\approx 1.5 - 2.5 \times 10^5 \text{ erg cm}^{-2} \text{ s}^{-1}$ . A large fraction of the coronal base energy input flux  $\phi_h$  estimated in this work, or even its totality, could then be accounted for by Alfvén waves.

Results of the AWSoM model are compared to those of the DENT reconstructions in the range of coronal heights  $\approx 1.05 - 1.20 R_\odot$  simultaneously covered by both models. In its current implementation, the AWSoM model can not reproduce down loops (type 0), so the comparison is restricted to type I, II and III field lines. The detailed comparison shown in this work can be summarized as follows. For CR-2082, the electron density of both models agree within  $\approx 20\%$  in most regions, while for CR-2208 the agreement is within  $\approx 5\%$ . The noticeable exception is to be found near the open/closed boundaries of both target rotations, where the disagreement between both models can be up to twice as much. In the case of the electron temperature, both models agree within  $\approx 10 - 15\%$  in all regions, for both target rotations, with larger discrepancies in the CHs. This level of agreement between both models is considerably better than that reported in previous works. Oran *et al.* (2015) and Jin *et al.* (2012) reported electron density values of the AWSoM model differing by  $\approx 50\%$  compared to the

DEMT reconstructions, both in the equatorial streamer and CH regions. **NOTE:** Chip, if Section 2.2 explains the most significant improvements of AWSoM since the version used in those references, we can comment on the reason for the improvement here. **Note by Diego:** Chip, Nishtha, if you think we can relate some differences or observed trends of AWSoM with the magnetic field, this could be a good place, but I need your insight here.

Within the quantitative match summarized in the previous paragraph, there are some qualitative agreements and disagreements between both models worth noticing. For both target rotations, the AWSoM model reproduces the relatively lower temperatures found by DEMT to characterize the low-latitudes of the equatorial streamer belt compared to its mid-latitudes. On the other hand, while the latitude of the open/closed magnetic boundary in both hemispheres matches the location of the strongest latitudinal gradient of the DEMT electron density, this is not the case for the AWSoM model, that shows a minimum density at the open/closed boundary. Also, while the DEMT electron density decreases from the open/closed boundary towards the poles (in both hemispheres of the two target rotations), the AWSoM model shows the opposite trend. This behavior is notoriously opposite to that reported in the AWSoM model version used by Oran *et al.* (2015), in which the electron density decreases from the open/closed boundary towards the poles. **NOTE:** Chip: Even if the match AWSoM/DEMT is quantitatively pretty good, this qualitative opposite behavior is off putting. Do you think there is room for improvement in the AWSoM model here? Maybe worth mentioning?

A detailed empirical description of the 3D thermodynamic structure of the inner corona at a global scale is currently only possible with tomographic techniques, such as DEMT. Using tomographic results for continuous validation of 3D MHD models is of high relevance for the continued improvement of models. In follow up articles we will carry out the 3D DEMT reconstruction and MHD modeling of new target rotations selected from the current solar minimum epoch between SCs 24 and 25, as well as rotation CR-2219 corresponding to the July 2nd 2019 total solar eclipse.

**Acknowledgments** D.G.Ll. and C.M.C. acknowledge CONICET doctoral fellowships (Res. Nr. 4870) to IAFE that supported their participation in this research. D.G.Ll, A.M.V., F.A.N. and C.M.C. acknowledge ANPCyT grant 2016/0221 to IAFE that partially supported their participation in this research. A.M.V. also acknowledges UBACyT grant 20020160100072BA to DCAO-UBA to FCEyN-UBA and IAFE that partially supported his participation in this research.

Disclosure of Potential Conflicts of Interest: The authors declare that they have no conflicts of interest.

## References

- Arge, C.N., Henney, C.J., Koller, J., Compeau, C.R., Young, S., MacKenzie, D., Fay, A., Harvey, J.W.: 2010, Air Force Data Assimilative Photospheric Flux Transport (ADAPT) Model. In: Maksimovic, M., Issautier, K., Meyer-Vernet, N., Moncuquet, M., Pantellini,

- F. (eds.) *Twelfth International Solar Wind Conference, American Institute of Physics Conference Series* **1216**, 343. DOI. ADS.
- Aschwanden, M.J.: 2004, *Physics of the Solar Corona. An Introduction*. ADS.
- Aschwanden, M.J., Schrijver, C.J.: 2002, Analytical Approximations to Hydrostatic Solutions and Scaling Laws of Coronal Loops. *Astrophys. J. Suppl.* **142**(2), 269. DOI. ADS.
- Chandran, B.D.G., Dennis, T.J., Quataert, E., Bale, S.D.: 2011, Incorporating Kinetic Physics into a Two-fluid Solar-wind Model with Temperature Anisotropy and Low-frequency Alfvén-wave Turbulence. *Astrophys. J.* **743**(2), 197. DOI. ADS.
- Del Zanna, G., Dere, K.P., Young, P.R., Landi, E., Mason, H.E.: 2015, CHIANTI - An atomic database for emission lines. Version 8. *Astron. Astrophys.* **582**, A56. DOI. ADS.
- Frazin, R.A.: 2000, Tomography of the Solar Corona. I. A Robust, Regularized, Positive Estimation Method. *Astrophys. J.* **530**, 1026. DOI. ADS.
- Frazin, R.A., Vázquez, A.M., Kamalabadi, F.: 2009, Quantitative, Three-dimensional Analysis of the Global Corona with Multi-spacecraft Differential Emission Measure Tomography. *Astrophys. J.* **701**, 547. DOI. ADS.
- Hahn, M., Savin, D.W.: 2014, Evidence for Wave Heating of the Quiet-Sun Corona. *Astrophys. J.* **795**(2), 111. DOI. ADS.
- Henney, C.J., Toussaint, W.A., White, S.M., Arge, C.N.: 2012, Forecasting F<sub>10.7</sub> with solar magnetic flux transport modeling. *Space Weather* **10**, S02011. DOI. ADS.
- Huang, Z., Frazin, R.A., Landi, E., Manchester, W.B., Vázquez, A.M., Gombosi, T.I.: 2012, Newly Discovered Global Temperature Structures in the Quiet Sun at Solar Minimum. *Astrophys. J.* **755**, 86. DOI. ADS.
- Jin, M., Manchester, W.B., van der Holst, B., Oran, R., Sokolov, I., Toth, G., Gombosi, T.I., Vourlidas, A., Liu, Y., Sun, X.: 2012, Simulate the Coronal Mass Ejection on 2011 March 7 from Chromosphere to 1 AU. In: *AGU Fall Meeting Abstracts* **2012**, SH33E. ADS.
- Landi, E., Young, P.R., Dere, K.P., Del Zanna, G., Mason, H.E.: 2013, CHIANTI - An Atomic Database for Emission Lines. XIII. Soft X-Ray Improvements and Other Changes. *Astrophys. J.* **763**, 86. DOI. ADS.
- Lemen, J.R., Title, A.M., Akin, D.J., Boerner, P.F., Chou, C., Drake, J.F., Duncan, D.W., Edwards, C.G., Friedlaender, F.M., Heyman, G.F., Hurlburt, N.E., Katz, N.L., Kushner, G.D., Levay, M., Lindgren, R.W., Mathur, D.P., McFeaters, E.L., Mitchell, S., Rehse, R.A., Schrijver, C.J., Springer, L.A., Stern, R.A., Tarbell, T.D., Wuelser, J.-P., Wolfson, C.J., Yanari, C., Bookbinder, J.A., Cheimets, P.N., Caldwell, D., Deluca, E.E., Gates, R., Golub, L., Park, S., Podgorski, W.A., Bush, R.I., Scherrer, P.H., Gumm, M.A., Smith, P., Auker, G., Jerram, P., Pool, P., Souffri, R., Windt, D.L., Beardsley, S., Clapp, M., Lang, J., Waltham, N.: 2012, The Atmospheric Imaging Assembly (AIA) on the Solar Dynamics Observatory (SDO). *Solar Phys.* **275**, 17. DOI. ADS.
- Lionello, R., Linker, J.A., Mikić, Z.: 2009, Multispectral Emission of the Sun During the First Whole Sun Month: Magnetohydrodynamic Simulations. *Astrophys. J.* **690**(1), 902. DOI. ADS.
- Lithwick, Y., Goldreich, P., Sridhar, S.: 2007, Imbalanced Strong MHD Turbulence. *Astrophys. J.* **655**(1), 269. DOI. ADS.
- Lloveras, D.G., Vázquez, A.M., Nuevo, F.A., Frazin, R.A.: 2017, Comparative Study of the Three-Dimensional Thermodynamical Structure of the Inner Corona of Solar Minimum Carrington Rotations 1915 and 2081. *Solar Phys.* **292**(10), 153. DOI. <https://doi.org/10.1007/s11207-017-1179-z>.
- Mac Cormack, C., Vázquez, A.M., López Fuentes, M., Nuevo, F.A., Landi, E., Frazin, R.A.: 2017, Energy Input Flux in the Global Quiet-Sun Corona. *Astrophys. J.* **843**, 70. DOI. ADS.
- Nuevo, F.A., Huang, Z., Frazin, R., Manchester, i. Ward B., Jin, M., Vázquez, A.M.: 2013, Evolution of the Global Temperature Structure of the Solar Corona during the Minimum between Solar Cycles 23 and 24. *Astrophys. J.* **773**(1), 9. DOI. ADS.
- Nuevo, F.A., Vázquez, A.M., Landi, E., Frazin, R.: 2015, Multimodal Differential Emission Measure in the Solar Corona. *Astrophys. J.* **811**(2), 128. DOI. ADS.
- Oran, R., Landi, E., van der Holst, B., Lepri, S.T., Vázquez, A.M., Nuevo, F.A., Frazin, R., Manchester, W., Sokolov, I., Gombosi, T.I.: 2015, A Steady-state Picture of Solar Wind Acceleration and Charge State Composition Derived from a Global Wave-driven MHD Model. *Astrophys. J.* **806**(1), 55. DOI. ADS.
- Powell, K.G., Roe, P.L., Linde, T.J., Gombosi, T.I., De Zeeuw, D.L.: 1999, A Solution-Adaptive Upwind Scheme for Ideal Magnetohydrodynamics. *Journal of Computational Physics* **154**(2), 284. DOI. ADS.

- Press, W.H., Teukolsky, S.A., Vetterling, W.T., Flannery, B.P.: 2002, *Numerical recipes in C++ : the art of scientific computing*. ADS.
- Sachdeva, N., van der Holst, B., Manchester, W.B., Tóth, G., Chen, Y., Lloveras, D.G., Vázquez, A.M., Lamy, P., Wojak, J., Jackson, B.V., Yu, H.-S., Henney, C.J.: 2019, Validation of the Alfvén Wave Solar Atmosphere Model (AWSOM) with Observations from the Low Corona to 1 au. *Astrophys. J.* **887**(1), 83. DOI. ADS.
- Schiff, A.J., Cranmer, S.R.: 2016, Explaining Inverted-temperature Loops in the Quiet Solar Corona with Magnetohydrodynamic Wave-mode Conversion. *Astrophys. J.* **831**(1), 10. DOI. ADS.
- Serio, S., Peres, G., Vaiana, G.S., Golub, L., Rosner, R.: 1981, Closed coronal structures. II - Generalized hydrostatic model. *Astrophys. J.* **243**, 288. DOI. ADS.
- Sokolov, I.V., van der Holst, B., Oran, R., Downs, C., Roussev, I.I., Jin, M., Manchester, W.B., Evans, R.M., Gombosi, T.I.: 2013, MAGNETOHYDRODYNAMIC WAVES AND CORONAL HEATING: UNIFYING EMPIRICAL AND MHD TURBULENCE MODELS. *apj* **764**(1), 23. DOI. <https://doi.org/10.1088%2F0004-637x%2F764%2F1%2F23>.
- Spitzer, L.: 1962, *Physics of Fully Ionized Gases*. ADS.
- Tóth, G., van der Holst, B., Sokolov, I.V., De Zeeuw, D.L., Gombosi, T.I., Fang, F., Manchester, W.B., Meng, X., Najib, D., Powell, K.G., et al.: 2012, Adaptive numerical algorithms in space weather modeling. *J. Comput. Phys.* **231**(3), 870–903. DOI. <https://doi.org/10.1016/j.jcp.2011.02.006>.
- van der Holst, B., Manchester, I. W. B., Frazin, R.A., Vázquez, A.M., Tóth, G., Gombosi, T.I.: 2010, A Data-driven, Two-temperature Solar Wind Model with Alfvén Waves. *Astrophys. J.* **725**(1), 1373. DOI. ADS.
- van der Holst, B., Sokolov, I.V., Meng, X., Jin, M., Manchester, I. W. B., Tóth, G., Gombosi, T.I.: 2014, Alfvén Wave Solar Model (AWSOM): Coronal Heating. *Astrophys. J.* **782**(2), 81. DOI. ADS.
- Vázquez, A.M.: 2016, Seeing the solar corona in three dimensions. *Advances in Space Research* **57**, 1286. DOI.
- Vázquez, A.M., Frazin, R.A., Kamalabadi, F.: 2009, 3D Temperatures and Densities of the Solar Corona via Multi-Spacecraft EUV Tomography: Analysis of Prominence Cavities. *Solar Phys.* **256**(1-2), 73. DOI. ADS.
- Vázquez, A.M., Frazin, R.A., Manchester, I. Ward B.: 2010, The Solar Minimum Corona from Differential Emission Measure Tomography. *Astrophys. J.* **715**(2), 1352. DOI. ADS.
- Worden, J., Harvey, J.: 2000, An Evolving Synoptic Magnetic Flux map and Implications for the Distribution of Photospheric Magnetic Flux. *Solar Phys.* **195**(2), 247. DOI. ADS.
- Wuelser, J.-P., Lemen, J.R., Tarbell, T.D., Wolfson, C.J., Cannon, J.C., Carpenter, B.A., Duncan, D.W., Gradwohl, G.S., Meyer, S.B., Moore, A.S., Navarro, R.L., Pearson, J.D., Rossi, G.R., Springer, L.A., Howard, R.A., Moses, J.D., Newmark, J.S., Delaboudiniere, J.-P., Artzner, G.E., Auchere, F., Bougnet, M., Bouyries, P., Bridou, F., Clotaire, J.-Y., Colas, G., Delmotte, F., Jerome, A., Lamare, M., Mercier, R., Mullot, M., Ravet, M.-F., Song, X., Bothmer, V., Deutsch, W.: 2004, EUVI: the STEREO-SECCHI extreme ultraviolet imager. In: Fineschi, S., Gumm, M.A. (eds.) *Telescopes and Instrumentation for Solar Astrophysics, Proc. SPIE* **5171**, 111. DOI. ADS.